ACS APPLIED MATERIALS & INTERFACES

Templating Sol–Gel Hematite Films with Sacrificial Copper Oxide: Enhancing Photoanode Performance with Nanostructure and Oxygen Vacancies

Yang Li,[†,‡] Néstor Guijarro,[‡] Xiaoli Zhang,[†] Mathieu S. Prévot,[‡] Xavier A. Jeanbourquin,[‡] Kevin Sivula,[*,‡] Hong Chen,[*,§] and Yongdan Li[†]

[†]Collaborative Innovation Center of Chemical Science and Engineering (Tianjin), Tianjin Key Laboratory of Applied Catalysis Science and Technology, State Key Laboratory of Chemical Engineering (Tianjin University), School of Chemical Engineering, Tianjin University, Tianjin 300072, China

[‡]Laboratory for Molecular Engineering of Optoelectronic Nanomaterials, École Polytechnique Fédérale de Lausanne (EPFL), Station 6, 1015 Lausanne, Switzerland

[§]School of Environmental Science and Engineering, Tianjin University, Tianjin 300072, China

S *Supporting Information*

ABSTRACT: Nanostructuring hematite films is a critical step for enhancing photoelectrochemical performance by circumventing the intrinsic limitations on minority carrier transport. Herein, we present a novel sol–gel approach that affords nanostructured hematite films by including CuO as sacrificial templating agent. First, by annealing in air at 450 °C a film comprising an intimate mixture of CuO and Fe_2O_3 nanoparticles is obtained. The subsequent treatment with NaCl and annealing at 700 °C under Argon reveals a nanostructured highly crystalline hematite film devoid of copper. Photoelectrochemical investigations reveal that the incorporation of CuO as templating agent and the inert conditions employed during the annealing play a crucial role in the performance of the hematite electrodes. Mott–Schottky analysis shows a higher donor concentration when annealing in inert conditions, and even higher when combined with the NaCl treatment. These findings agree well with the presence of an oxygen-deficient shell on the material's surface evidenced by FT-IR and XPS measurements. Likewise, the incorporation of the CuO enhances the photocurrent obtained at 1.23 V from 0.55 to 0.8 mA·cm^{-2} because of an improved nanostructure. Optimized films demonstrate an incident photon-to-current efficiency (IPCE) of 52% at 380 nm when applying 1.23 V versus RHE, and a faradaic efficiency for water splitting close to unity.

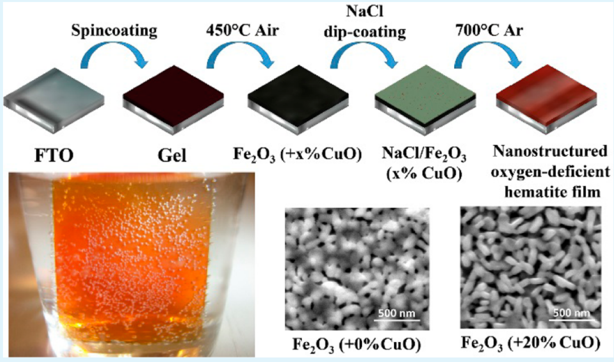

KEYWORDS: *hematite, water splitting, photoelectrochemistry, sol–gel, copper oxide*

1. INTRODUCTION

Hematite (α-Fe_2O_3) is currently under intense development as a water-oxidizing photoanode material for direct photoelectrochemical (PEC) solar fuel production, which has a favorable bandgap of about 2.2 eV and a high stability against photo- and chemical corrosion in alkaline electrolytes.[1] On the basis of the optical properties of hematite and the standard solar spectrum, the solar-to-hydrogen efficiency of PEC tandem cell with a hematite photoanode could be as high as 15%.[2,3] However, the practical performance of hematite in solar water splitting reaction is still lagging far behind the theoretical maximum because of several limiting factors, such as the poor conductivity, short lifetime of the excited-state carriers (10^{-12} s), poor oxygen evolution reaction (OER) kinetics, and short hole diffusion length (2–4 nm).[4−8]

Generally, three different strategies are envisaged to solve the aforementioned problems and obtain highly efficient hematite films. First, increasing the interfacial area between the electrolyte and hematite film would facilitate the charge collection by enhancing the probability that an absorbed photon is within the hole transport length to the semiconductor–liquid junction.[9,10] Therefore, nanorods, nanowire arrays, nanonets, and porous colloidal based films are attractive morphologies for a high photon harvesting efficiency.[11−13] However, realizing a high surface area does not improve the intrinsic optical and electronic properties of the electrode material. Another strategy to improve the performance of hematite photoanodes is to increase the majority carrier concentration through the use of n-type subsitutional dopants (e.g., Si^{4+}, Pt^{4+}, Ti^{4+}, Nb^{5+}, or Sn^{4+})[14] or by increasing the

Received: March 10, 2015
Accepted: July 17, 2015
Published: July 17, 2015

DOI: 10.1021/acsami.5b02111
ACS Appl. Mater. Interfaces 2015, 7, 16999−17007

density of the oxygen vacancies (which are known to serve as shallow donors for n-type oxides such as TiO_2, WO_3, and α-Fe_2O_3).[15,16] Besides, surface properties are extremely vital for water splitting reaction, therefore, the performance of hematite can be improved with surface decoration. For example Co-Pi and IrO_2, among others, are reported to be efficient cocatalysts on hematite surface,[17] and surface trapping states can be passivated with various overlayers.[18]

To date, the best-performing hematite films in the absence of cocatalyst have been reported to be prepared by means of the so-called atmospheric pressure chemical vapor deposition (APCVD), displaying an anodic photocurrent over 2.5 mA cm^{-2} at 1.23 V versus RHE.[8] However, this approach requires costly instruments, the use of toxic precursors together with a tight control on numerous parameters involved during the deposition of the film. Consequently, alternative cost-effective approaches for the fabrication of nanostructured hematite electrodes have been concurrently studied, such as hydrothermal or sol−gel routes, though the anodic photocurrents still lag behind those reported by APCVD. Ling et al.[19] reported Sn-doped hematite nanostructures prepared by hydrothermal methods displaying anodic photocurrents of 1.8 mA cm^{-2} at 1.23 V vs RHE. More recently, Kim et al.[4] prepared worm-like hematite photoanodes that attained 1.26 mA cm^{-2} (undoped) and 2.16 mA cm^{-2} (doped with Pt) at 1.23 V vs RHE. However, the hydrothermal approaches are not suitable for large-scale roll-to-roll solution processing which would hold the key for lowering the fabrication costs. On the other hand, sol−gel procedures have emerged as enticing alternatives to the hydrothermal method paving the way for a solution-processable and easily scalable fabrication of films. Hamd et al.[3] reported the fabrication of mesoporous films of hematite by a sol−gel method displaying anodic photocurrents of ∼0.45 mA cm^{-2} at 1.23 V vs RHE. Likewise, Frydrych et al.[20] demonstrated the addition of a Sn precursor during the thin film deposition enables the Sn-doping reaching photocurrents close to 0.4 mA cm^{-2} at 1.23 V vs RHE when annealing at relatively low temperatures (650 °C vs the commonly used 750−800 °C).

Apart from lowering the fabrication cost of the hematite films, designing new and easily scalable nanostructuring approaches to overcome the charge transport limitations within the hematite would be desirable. However, the high temperatures (750−800 °C) employed in the preparation of the more active hematite thin film promotes a strong sintering, losing, in turn, the nanosized features. In an attempt to overcome this problem, Brillet et al.[21] reported a multistep approach to circumvent the coalescence of the hematite nanostructure that occurs at 800 °C, which involves a two-step annealing (the first at 450 °C, to develop the mesoporous structure, and the second, at 800 °C to improve the crystallinity and connectivity) and a coating in-between with rigid SiO_2 shell to prevent the collapse of the structure. In other cases, such as in the hydrothermally prepared worm-like structure, an increase in the size of the nanoscopic features is clearly noticed upon annealing, which might limit the performance.[4]

Herein, we report a facile, cost-effective and versatile sol−gel method for the fabrication of oxygen-deficient nanostructured hematite films that exhibit the highest anodic photocurrents among the state-of-the-art sol−gel processed hematite thin films. In this work, the iron oxide precursor is combined with a copper oxide precursor, spin-coated and submitted to a two-step annealing, the first one (450 °C) to create an intimate mixture Fe_2O_3/CuO and, the second one to produce the nanostructured hematite (700 °C). The removal of the CuO at high temperatures in the presence of NaCl induces the growth of highly crystalline hematite with a defined nanostructure that benefits the water photo-oxidation performance. The effects of the annealing atmosphere and treatments as well as of the morphology on the photoelectrochemical response of the hematite films are analyzed.

2. MATERIALS AND METHODS

2.1. Hematite Photoelectrode Fabrication. $Fe(NO_3)_3{\cdot}9H_2O$ (Acros, 99+%), $Cu(NO_3)_2{\cdot}3H_2O$ (Sigma-Aldrich, 99−104%), citric acid (Alfa Aesar, 99+%), ethylene glycol, and ethanol (Fluka, 99.8%) were used in the synthesis. Transparent conducting substrate of F:SnO_2 (FTO) deposited on aluminoborosilicate glass was purchased from Solaronix SA, and successively washed with Hellmanex III (alkaline cleaning agent), acetone, and ethanol.

In a typical experiment, $Fe(NO_3)_3{\cdot}9H_2O$ (2.00 mmol), citric acid (4.00 mmol), and an amount of $Cu(NO_3)_2{\cdot}3H_2O$ (x mmol, $0 < x < 2$) were mixed in 10 mL of ethanol. After it was stirred for 2 h, ethylene glycol (4.48 mmol) was added to the mixture, which was stirred for another 1 h. The resulting solution was spin coated onto clean FTO substrate at 3000 rpm for 1 min. The resulting films were dried on a hot plate at 100 °C for 10 min, and then annealed in air at 450 °C in muffle furnace (ramp rate: 10 °C·min^{-1}) for 1 h to remove the traces of organic material. Successive layers were then deposited on top of the first one following the same steps. Finally, the precursor films were annealed under air or argon flow (300 mL·min^{-1}) at 700 °C in a 5 cm diameter tube furnace (ramp rate: 10 °C min^{-1}) for 2 h.

For preparing the nanostructured hematite films, the precursor films were prepared and annealed in air at 450 °C, similar to the above procedures. Afterward, the sample was dipped in a saturated aqueous solution of NaCl and dried in air. Then the films were annealed under argon flow (300 mL·min^{-1}) at 700 °C for 2 h. Finally, the hematite films were washed with ultrapure water to remove the excess NaCl.

2.2. Characterization. UV−vis total reflectance spectra of hematite thin films were recorded with a UV−vis-NIR UV-3600 (Shimadzu) Spectrophotometer, equipped with an integrating sphere. X-ray diffraction (XRD) patterns of the thin films were obtained with a D8 Discovery (Bruker) diffractometer equipped with a Cu Kα X-ray source, in a geometry where the X-ray source was fixed, and the detector scanned a set range of angles (20−90°). The scanning electron microscopy (SEM) images were obtained with a Zeiss Merlin microscope. The iron oxidation states were analyzed with an X-ray photoelectron spectroscope (XPS) Perkinelmer, PHI1600 ESCA. The binding energy was calibrated using the C 1s photoelectron peak at 284.6 eV as the reference and the baseline of the Fe 2p spectra was fit with the Shirley algorithm. Nitrogen adsorption−desorption measurements were performed at 77 K on a Quantachrome QuadraSorb SI system to obtain the Brunauer−Emmett−Teller (BET) surface areas. The atomic force microscope (AFM) images were obtained with tapping mode AFM in air. The temperature and humidity during the test were 25 °C and 57%, respectively. A SNL10-A cantilever probe (Bruker) was used for characterizing. The absence of copper ions in the hematite films was further confirmed by an ICP-OES instrument (Vista-MPX). Briefly, the nanostructured hematite films were dissolved in in diluted nitric acid at 60 °C for 48 h, which was subsequently analyzed by ICP-OES correlating the signal with the corresponding calibration lines.

Electrochemical measurements were performed in a three-electrode Cappuccino-type cell using a computer controlled SP-200 potentiostat (BioLogic). All the potentials were measured against and referred to an Ag/AgCl/KCl (saturated) reference electrode (0.197 V vs SHE), while a Pt wire was used as a counter electrode. All the potentials were referred to the reversible hydrogen electrode (RHE), according to the following equation:

$$E(\mathrm{RHE}) = E(\mathrm{Ag/AgCl}) + 0.197 + 0.059 \times \mathrm{pH} \qquad (1)$$

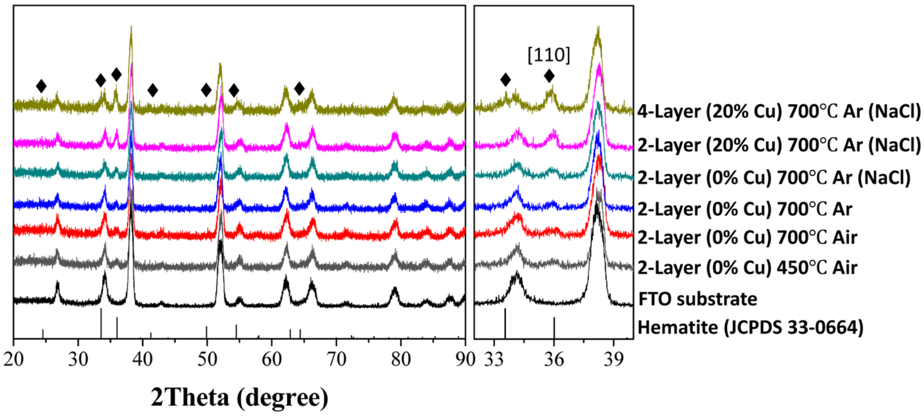

Figure 1. XRD patterns of the hematite thin films on FTO substrates prepared under different conditions.

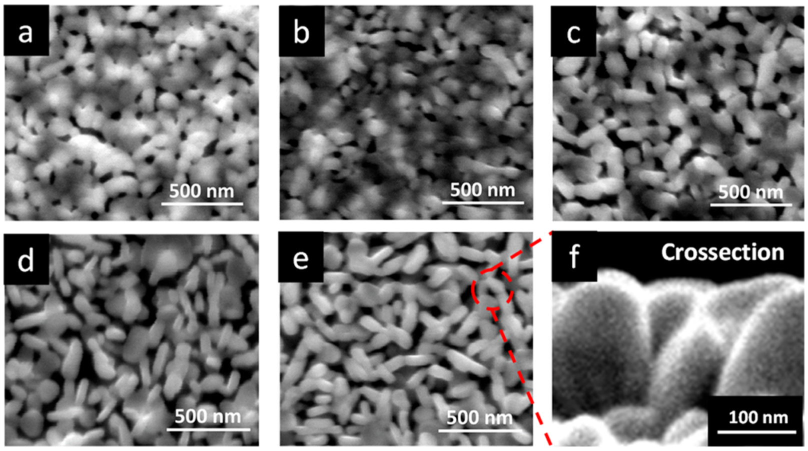

Figure 2. Top view SEM images for the 2-layer samples anneal at 700 °C in air (0% Cu) (a), in argon (0% Cu) (b), in argon with NaCl (0% Cu) (c), and argon with NaCl (20% Cu) (d). Top view SEM image for the 4-layer sample annealed at 700 °C in argon with NaCl (20% Cu) (e) and the corresponding cross-section (f).

The active geometric area of the electrode was 0.25 cm^2. All the measurements were carried out in aqueous 1 M NaOH electrolyte prepared with ultrapure (Milli-Q) water. Electrochemical Impedance Spectra (EIS) experiments were performed in the dark and under illumination at a frequency range of 100 mHz−0.1 MHz. Illumination in photoelectrochemical measurements was provided by a 500 W Muller Electronik Xenon-arc lamp, calibrated to provide 1 sun (AM 1.5G, 100 mW cm^{-2}) as reported elsewhere.[22] The measurement of H_2 and O_2 was carried out by connecting the photoelectrochemical cell to sealed system to circulate the gas toward the gas chromatograph (GC, Perkinelmer Clarus 500, TCD detector, carrier gas = Ar; flow rate = 36 mL/min; oven temperature = 50 °C; detector temperature = 120 °C with Ar as the carrier gas) for the analysis. The sealed system was previously vacuumed to evacuate the air and the dissolved oxygen.[23,24] The explanation of the determination of the faradaic efficiency is provided in the Supporting Information.

3. RESULTS AND DISCUSSION

3.1. Composition and Crystal Structure. The templated sol−gel method for the synthesis of nanostructured hematite films was fortuitously found during our research on copper−iron oxide (delafossite) thin films.[22] The copper−iron oxide was prepared by successively spin-coating a solution containing iron oxide and copper oxide precursors that, were sequentially annealed at 450 °C to create an intimate mixture of the oxides and finally annealed under oxygen-deficient atmosphere at 700 °C to synthesize the delafossite structure. In an attempt to enhance the crystallinity of the copper−iron oxide, the sample was dipped in a saturated solution of NaCl prior the last thermal treatment. NaCl has been widely employed as an agent for promoting grain growth and improved crystallization of many materials, such as hematite[25] or $CuInGaSe_2$,[26] among others. Intriguingly, a phase pure hematite film resulted from this treatment, instead of a higher crystalline copper−iron oxide film. More importantly, no trace of Cu or Na was found by XPS (Supporting Information Figure S1). We applied ICP-OES for further confirmation, and no trace of copper was found (results not shown). It is important to note that Sn was detected in the XPS spectra (Supporting Information Figure S1), which is known to effectively dope the hematite enhancing the PEC response.[27] However, as shown in Supporting Information Figure S1 the relative Sn:Fe atomic concentration is around 3:100, far below the optimum ratio of 20:100 reported by Frydrych et al.[28] Probably, the annealing performed at 700 °C is not enough to cause noticeable diffusion of Sn atoms into the α-Fe_2O_3 as previously reported. Likewise, XRD patterns shown in Figure 1 confirm that α-Fe_2O_3 single phase (JCPDS 33-0664) was successfully prepared, without signals corresponding to the CuO. To further confirm this surprising result, a control experiment where the sol−gel, devoid from the iron precursor, was employed to prepare thin films of CuO and was submitted to the same annealing treatment with NaCl. Unambiguously, the brownish CuO film was completely removed from the substrate, and no signal, except the substrate, was detected by

Raman spectroscopy (result not shown). The melting point of CuO is around 1326 °C, and the control experiments showed that CuO cannot be removed at 700 °C no matter in air or in Ar. It should also be pointed out that in the absence of NaCl, CuO converted into Cu_2O remaining on the substrate after the annealing in Ar as confirmed by XRD (Supporting Information Figure S2).[29] Although CuO is clearly removed when NaCl is present during the annealing under inert conditions, the mechanism remains elusive. We hypothesize that the CuO reacts with the NaCl producing volatile compounds such as CuCl and Na_2O_2 that are carried by the argon gas flowing through the tubular oven. Experiments to better understand the removal of CuO are underway and will be published on due course.

In view of Figure 1, it is shown that the α-Fe_2O_3 crystal structure is detected when annealing at temperatures as low as 450 °C, and the intensity of the [110] peak is markedly high compared to the other peaks of the hematite films. The annealing at higher temperature (700 °C) does not induce significant changes in the XRD. However, the annealing in the presence of NaCl under inert conditions showed more intense peaks, which correlates well with an improved crystallinity assisted by the NaCl, as reported elsewhere.[25]

3.2. Morphology and Optical Absorption Property.

The removal of CuO in the presence of NaCl as established above provides a rational route to nanostructure the hematite films during annealing. As observed, in the absence of copper precursor, the annealing at 450 °C produced a thin film where voids emerge from the shrinkage of inorganic material and the removal of solvent and organic compounds, shown in Supporting Information Figure S3. The BET data showed the surface area of the hematite films (450 °C) was around 0.77 m^2 on 1 cm^2 of FTO substrate, and the surface roughness was determined to be 6.8 nm by AFM. Subsequent annealing at higher temperature (700 °C, Figure 2a) gave a more compact structure because of sintering but still retained some voids, which also results in slightly decreased surface areas of 0.71 m^2 and 0.73 m^2 per cm^2 (geometric area) of FTO substrate, in air and Ar, respectively. The AFM data reflected that the roughness were 8.8 and 14 nm, in air and Ar, respectively. The incorporation of NaCl did not lead to significant changes in the morphology of the films prepared from precursors devoid from copper precursor, but produced a decreased surface area of 0.55 m^2 per cm^2 of FTO substrate, and the AFM data showed that the surface roughness was 19 nm. When the copper precursor is included, the composite CuO/Fe_2O_3 thin film obtained after annealing at 450 °C shows a significantly more continuous film, however, some voids exposing the substrate were still noticeable (Supporting Information Figure S3). Annealing under argon after the NaCl treatment gave rise to a markedly different morphology with a more open structure (Figure 2c–f). The top view and the cross section suggest a columnar structure for the as-grown crystals, with a clear and extended spacing in-between the different grains of ~100 nm, and the surface area increases up to 1.2 m^2 per cm^2 of FTO, and the surface roughness was determined to be 28 nm. It should be borne in mind that while Cu and Fe are initially well-mixed, only well crystalline α-Fe_2O_3 columns remain after annealing. We speculate that the high temperatures combined with the NaCl favored the coalescence of α-Fe_2O_3 grains inducing the grain growth oriented by the CuO. It would be reasonable to consider that in such conditions CuO is simultaneously segregated and removed by reaction with NaCl. In such a manner, the lack of α-Fe_2O_3 particles that fed the columnar grains growth would also account for the more opened structure of the hematite films prepared with CuO and NaCl. AFM images show that replacing the air by argon for the annealing indeed induce larger features and a clearly higher roughness (Supporting Information Figure S4). By including the NaCl treatment an additional increased particle size is detected. Interestingly, the addition of the CuO template with NaCl leads to a significantly more open structure. Furthermore, from the cross-sectional SEM images (Supporting Information Figure S5), we observe that the thicknesses of the resulting 2-layer hematite films were ca. 100 nm, while the thickness of the 4-layer samples was ~200 nm (Figure 2f). Interestingly, the change in the morphology can be easily noticed in the cross-sectional image. It is worth mentioning that the thickness is significantly below the ca. 500 nm that has been reported for more efficient hematite films.[30]

The copper percentage discussed until now (20%) is that which demonstrated the optimum PEC performance (vide infra). However, the effect of the copper content has proven to affect the morphology of the resulting films (Supporting Information Figure S6). Increasing the copper content from 10% to 40% appears to increase the dimensions of the hematite grains besides the spacing in between the different columnar grains of hematite. This is not unexpected given that a larger amount of copper would constraint more the hematite phase when the copper is removed during the annealing treatment.

The effects of the different annealing treatments on the light absorption were monitored by using UV–vis spectroscopy. As shown in Supporting Information Figure S7, the UV–vis total reflectance spectra for the different hematite films as a function of the preparation route are presented. The choice of the total reflectance instead of the common absorbance or transmittance was in response to the necessity of comparing films with different scattering/reflective properties. By using the total reflectance configuration, all the unabsorbed photons, viz. reflected and scattered, would not be erroneously considered as absorbed. The deposition of hematite films prompted a sharp decrease in the reflectance from 600 nm that extended toward lower wavelength (520 nm). In order to determine the band gap of the hematite films as a function of the presented treatments, a Tauc analysis was employed (see Supporting Information Figure S8 and S9). It was found that the direct optical band gap of hematite thin films slightly change from 2.18 to 2.14 eV when annealed with NaCl or when including the sacrificial template. Likewise, the indirect optical band gap change from 2.11 to 2.10 eV when annealed with NaCl or when including the sacrificial template. This matches quite well with the absorbance[31] and band gap[32] reported elsewhere. The spectra of the films annealed in the absence of NaCl virtually gave higher reflectance values than those annealed with NaCl. Interestingly, the apparent higher light absorption of the films treated with CuO template and NaCl could reasonably result from the improved light scattering of these films due to the increased roughness.[33] As expected, the reflectance further decreased with the increase of the film thickness. In this case the tail of absorption extends to 700 nm, well-below the expected onset of light absorption which would be likely attributed to the enhanced light scattering from the film. Note that the bands that appear between 300 and 520 nm are commonly originated from the thin-film interference between the hematite, FTO and the glass substrate.

3.3. Effects of Inert Atmosphere and NaCl Overlayer on Photoelectrochemical Properties. In Figure 3a, the corresponding water oxidation photocurrent densities of the hematite films devoid from copper but with different annealing conditions are presented. The hematite film annealed at 450 °C in air showed negligible photocurrent values in the potential range scanned. Subsequent annealing at 700 °C in air induced a rather insignificant enhance in the photoelectrochemical performance, delivering photocurrent densities close to 0.05 mA·cm^{-2} at 1.23 V vs RHE, which are close to other hematite films reported elsewhere.[3,34,35] Interestingly, following the same recipe but annealing in Ar, the hematite films exhibited a dramatic increase in the photoelectrochemical response delivering photocurrent densities of 0.4 mA·cm^{-2} at 1.23 V vs RHE. It is worth mentioning that the annealing treatments of hematite films under inert or oxygen-deficient atmospheres have been already proposed by some authors as a feasible route to increase the oxygen vacancies, and hence, the donor densities on the film and the overall performance.[36,37] Additionally, the NaCl treatment increased the recorded photocurrent up to 0.55 mA·cm^{-2} at 1.23 V vs RHE, and more significantly at larger bias, that is, from 1 to 1.7 mA·cm^{-2} at 1.6 V vs RHE.

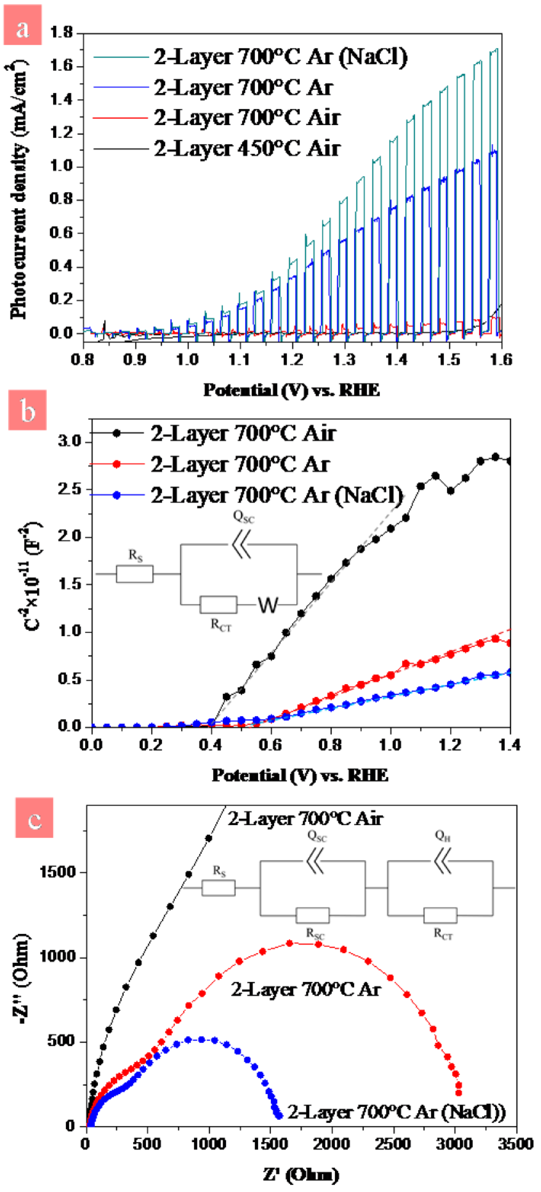

Figure 3. Photoelectrochemical properties of the hematite films. (a) The 2-layer hematite films heated at different temperature and in different atmosphere, illuminated from the front; (b) Mott–Schottky plots of the 2-layer hematite films heated in different atomsphere; (c) Nyquist impedance plots of the 2-layer hematite films under illumination.

To investigate the mechanism behind the enhancement of the photocurrent density, Mott–Schottky analysis was carried out in the dark on the hematite films. A simple Randles circuit model (inset of Figure 3b) was used to fit the impedance data and extract the space-charge capacitance (C_{SC}). For an n-type semiconductor, plotting C_{SC}^{-2} vs potential (E) should produce linear data that intersects the x-axis at the so-called flat-band potential (V_{FB}) and whose slope is inversely proportional to the donor concentration (N_D) (see Supporting Information). The hematite films annealed at 700 °C in air showed a linear Mott–Schottky behavior between 0.4 and 0.9 V vs RHE (Figure 3b). A linear fit in this range led to an estimation of the flat-band potential at 0.4 V vs RHE and a donor concentration of 1.9×10^{20} cm^{-3}. In contrast, the films annealed in Ar and the NaCl treated films both had lower flat-band potentials (0.52 V vs RHE) and much smaller slopes than the film annealed in air, indicating much higher donor concentrations in these hematite films, which were determined as 7.0×10^{20} and 1.3×10^{21} cm^{-3}, respectively, which is in agreement with previously reported increase in donor density when annealing in oxygen-deficient atmospheres.[36] These findings suggest that heating in inert atmosphere and the NaCl treatment can increase the charge carrier density by up to an order of magnitude. Indeed the change in the photoelectrochemical response of the hematite electrodes submitted to the different annealing positively correlates with an increase in the majority carrier concentration.[36] Interestingly, the donor concentrations found for our electrodes are higher than those reported for other hematite electrodes. Indeed, donor concentration values of 9.5×10^{19},[38] 5.38×10^{19},[19] and 3.91×10^{18} cm^{-3}[4] have been reported for Ti-, Sn-, and Pt-doped hematite films, respectively. These examples correspond to representative examples of hematite electrodes since display the best performances to date. However, higher values were recently reported by Kim et al.[39] for ultrathin (30 nm) hematite photoanodes reaching values of 1.3×10^{22} cm^{-3}, which is the highest value reported to date. Note as well that as we mentioned before, the amount of Sn found by XPS in the hematite is rather insufficient to contribute to the improved performance.

The EIS performed under dark conditions contains valuable information on the electrical properties of the semiconductor/electrolyte interface, i.e. space charge layer, as well as on the charge transfer processes occurring at the interface and on semiconductor bulk properties. However, additional information especially regarding the role of surface states in charge transfer processes and recombination, is well-known to be extracted when performing the EIS under illumination.[40,41] The Nyquist plots under illumination (and at 1.16 V vs RHE) presented in Figure 3c show two semicircles. We used an equivalent circuit composed of 2 RC elements in series, which account for the semiconductor and surface processes, respectively, shown in the inset of Figure 3c. Since electronic processes in the bulk are normally faster than charge transfer processes or the diffusion of ions in solution, the low frequency response is assigned to the semiconductor-electrolyte charge transfer resistance (R_{CT}) together with the Helmholtz capacitance (C_H), while the high frequency response is accordingly designated to events occurring in the semiconductor with a space charge region resistance (R_{SC}) and the corresponding space-charge capacitance (C_{SC}).[42] After fitting the low frequency semicircles in Figure 3c, we find that the hematite films annealed in air have a R_{CT} as high as 25 kΩ, but the resistance decreased to 2.7 kΩ after heating in Ar. Heating the hematite films with a NaCl overlayer in Ar, the resistance can be further reduced to 1.3 kΩ. The decreasing R_{CT} suggests that photoexcited holes can reach the surface and react with water more easily.

3.4. Effects of Nanostructure on Photoelectrochemical Properties. As discussed above, the annealing conditions, that is, argon atmosphere and NaCl treatment led to significant improvements in the photoelectrochemical responses, likely related to the induced oxygen vacancies and the improved crystallinity of the films. In Figure 4a the effect of the copper loading on the photoelectrochemical performance of 2-layer samples is tracked by monitoring the j-V curves under chopped-light illumination. As observed, higher photocurrents are systematically obtained in the whole potential range when the copper content increases up to 20%, but excess of the copper affects adversely to the performance. Indeed, the photocurrent measured at 1.23 V vs RHE increases from 0.55 mA·cm^{-2} (0% Cu) up to 0.8 mA·cm^{-2} (20% Cu). Note that back and front illumination give rise to similar results (Supporting Information Figure S10a).

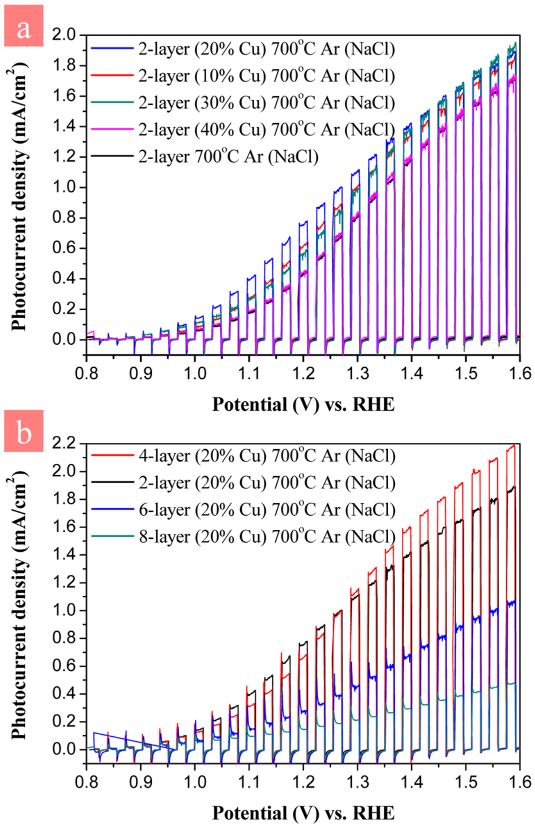

Figure 4. Photoelectrochemical properties of the hematite films. (a) The 2-layer hematite films containing various ratioes of CuO template, illuminated from the front. (b) The hematite films with different thickness, illuminated from the front.

To maximize the performance of the films prepared by using this novel templated sol−gel method, the thickness of the films was optimized. Figure 4b shows the *j*−*V* curves for films containing 20% copper but with the number of layers ranging from 2 to 8 layers. It should be borne in mind that increasing the thickness of the hematite films would improve the light harvesting but, concomitantly, it would enhance the recombination given the short carrier diffusion length on the hematite films. As observed the 2- and 4-layer samples exhibited similar performance. The photocurrent values near the onset were slightly higher for the 2-layer samples, and the corresponding values at higher potentials were better for the 4-layer sample. The improved light absorption accounts for the higher photocurrent obtained at large bias for the sample of 4-layers, but the obvious transient photocurrent spikes for this sample at low bias evidence the increased recombination when increasing the thickness of the films. In fact, as expected, the photocurrent values fell dramatically when increasing the thickness to 6- and 8-layer films. These results would be attributed to the larger distance that photogenerated carriers have to travel before reaching the interface, which critically enhances the probability of recombination.

3.5. Incident Photon-to-Current Efficiency and Oxygen Evolution Activity. The incident photon-to-current efficiency (IPCE) recorded for the 4-layer hematite sample templated with 20% copper content at 1.23 V vs RHE is presented in Figure 5a. As observed the IPCE matches quite well with the light absorption of the films, e.g. both absorption onset and IPCE onset closed to 600 nm. We note that the profile of the IPCE spectrum differs from that of finely nanostructured hematite, which exhibited higher values between 500 and 600 nm,[30] but was similar to that reported for hematite structures with similar features size[4] which gave an enhanced response in the near UV region. Indeed, the IPCE reached a maximum value of 52.2% at 380 nm, which is, to the best of our knowledge the highest value reported for hematite photoanodes prepared by sol−gel methods. Note that integrated photocurrent density from the IPCE spectrum gave rise to 1.7 mA·cm^{-2} which is higher than the one obtained in the j-V curves with a Xe lamp (0.8 mA·cm^{-2} at 1.23 V vs RHE). This different could be attributed to the spectral mismatch between the AM 1.5 solar spectrum and that of the Xe lamp employed for the *j*−*V* measurements. For the sake of comparison, we note that the state-of-the-art IPCE values are close to 60%, and have been recently attained with hematite films prepared by hydrothermal methods, doped with Pt, and combined with a cocatalyst.[4] It is reasonable to consider that the incorporation of cocatalysts in our system would further increase the IPCE values and the corresponding anodic photocurrents. These experiments are currently underway in our laboratory.

The stability of the hematite photoanode was analyzed by chronoamperometry under chopped-light illumination with an applied potential of 1.6 V vs RHE (inset, Figure 5a). After 1 h no significant degradation on the photocurrent value was detected. To further confirm that photocurrent values correspond to water oxidation reaction, the H_2 and O_2 evolving from the surfaces of the Pt counter electrode and the hematite, respectively, at an applied potential of 1.6 V vs RHE are shown in Figure 5b. About 40.2 and 20.1 μmol of H_2 and O_2 were collected during 1 h, respectively, showing the expected linear

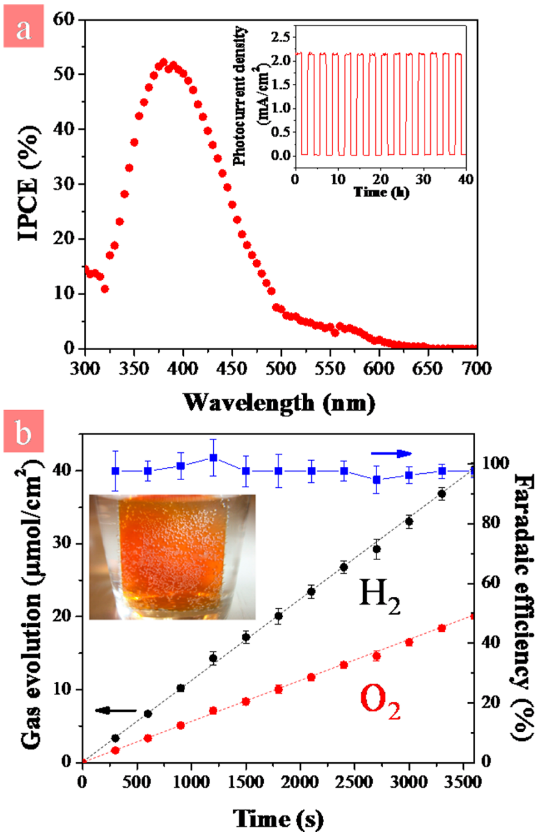

Figure 5. (a) IPCE of the 4-layer hematite (20% CuO) films (1.23 vs RHE in 1 M NaOH). Inset: The stability of the photocurrent density of the 4-layer hematite (20% CuO) films (1.6 vs RHE in 1 M NaOH under 100 mW/cm^2 illumination). (b) Gas evolution rate and the faradaic efficiency of the 4-layer hematite (20% CuO) films. Reaction conditions: 1.6 vs RHE in 1 M NaOH under 100 mW/cm^2 illumination.

increase in the evolving gas. From Figure 5c, we can see the faradaic efficiency fluctuates slightly, whose value are between 97% and 100%.

3.6. Mechanism. The Fe 2p XPS spectra of the hematite films are shown in Figure 6. As observed the Fe 2p peak split into two due to spin−orbit coupling (Fe $2p_{1/2}$, Fe $2p_{3/2}$) accompanied by the appearance of satellite peaks in this range. Particularly, for FeO a satellite peak linked to the Fe^{2+} emerges 4.5 eV above the Fe $2p_{3/2}$ component, whereas a peak 8 eV above the Fe $2p_{3/2}$ was reported for Fe_2O_3, presumably connected to the surface Fe^{3+}.[43] Close inspection of the XPS spectra revealed that in the absence of NaCl or copper template and regardless the annealing atmosphere (air or argon) there was only one satellite peak located at 719.3 eV, which correlated well with the oxidation state +3 for the surface Fe. However, annealing in Ar combined with the NaCl treatment triggered the appearance of another satellite peak closer to the Fe $2p_{3/2}$ component centered at 717.2 eV, which could be attributed to the oxidation state of +2 for the surface Fe, and the surface Fe(II) percentage was estimated to be 50%. Considering the rhombohedral crystal structure of hematite, we present the projection on the [110] plane of the hematite structure in Supporting Information Figure S11a. There are two types of oxygen states on hematite surface, that is, bridging hydroxyls (HO_{br}) and terminal hydroxyls (HO_t). This suggests that surface structure had changed when annealing the hematite films in the inert gas environment, and furthermore, surface hydroxyls can be mostly removed with the NaCl overlayer. The incorporation of the copper template clearly enhances the signal of the satellite peak closer to the Fe $2p_{3/2}$ signal related to Fe^{2+}, whose surface Fe(II) percentage was estimated to be 80%. These results suggest that NaCl treatment and especially the introduction of the CuO as a template bring about a Fe^{2+}-rich surface (Supporting Information Figure S11b). This indeed correlates well with increased charge carrier density discussed above, which could originate from the oxygen vacancies on the surface. Although no significant differences are detected when comparing the samples annealed under argon or air (note that the increase in the density of oxygen vacancies (Fe^{2+}) when annealing under inert atmospheres has been previously shown[35]) the remarkable enhancement in photoelectrochemical behavior after annealing in argon could be attributed to the formation of oxygen vacancies in the bulk.

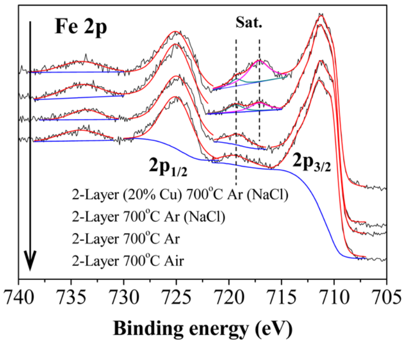

Figure 6. (a) FT-IR absorption spectra of the hematite films; (b) Fe 2p XPS spectra of the hematite films.

4. CONCLUSION

The sol−gel technique is known to be a reliable and easily solution-based route to prepare hematite films, though the performance of such electrodes are lagging far behind those reported for other fabrication routes such as APCVD or hydrothermal methods, mostly because of the larger feature size of the films. Herein, we reported a templated sol−gel approach that allows fabrication of nanostructured oxygen-deficient hematite films by incorporating CuO as a sacrificial template agent. Annealing treatments under inert conditions at 700 °C proved to increase donor densities by EIS measurements. Analogous annealing conditions but including CuO, induced a columnar-like crystal growth in the presence of NaCl which both promotes a better crystallinity and removes the copper oxide template, as evidenced the HR-SEM images and the XRD patterns, and simultaneously enhances the density of oxygen vacancies (Fe^{2+}) in the film. The photoelectrochemical characterization provided compelling evidence of the beneficial effect of both the NaCl and the inert atmosphere during the annealing, leading to a dramatic enhance of the photocurrents from 0.05 to 0.55 mA·cm^{-2} at 1.23 V vs RHE for 2-layer hematite films. Likewise, an optimized 4-layer sample (20% Cu) delivered an IPCE value of 52.2% (380 nm) at 1.23 V vs RHE, close to the maximum state-of-the-art values and well-above those reported by non-templated sol−gel routes. Moreover, O_2 evolution demonstrated to occur with a faradaic efficiency close to unity. Overall these findings provide a new pathway for preparing efficient hematite photoanode by using an easily scalable sol−gel route. Further insights by using transient absorption spectroscopy would potentially shed some light on the charge carrier transport and recombination processes,[44,45] evidencing, in turn, differences with other nanostructures. We hope that the encouraging performance of the hematite films prepared by this templated sol−gel approach will be further improved, especially, by coupling with state-of-the-art electrocatalyst for water oxidation such as IrO_2 or Co-Pi.

■ ASSOCIATED CONTENT

Supporting Information

Details of the complementary SEM images, XPS data, PEC performance, XRD patterns, UV−vis total reflectance spectra, and EIS analysis. The Supporting Information is available free of charge on the ACS Publications website at DOI: 10.1021/acsami.5b02111.

■ AUTHOR INFORMATION

Corresponding Authors

*Tel.: +41 21 693 79 79. E-mail: kevin.sivula@epfl.ch.
*Tel.: +86-22-27409405. Fax: +86-22-27409405. E-mail: chenhong_0405@tju.edu.cn.

Notes

The authors declare no competing financial interest.

■ ACKNOWLEDGMENTS

This work has been supported in part by the Program of Introducing Talents to the University Disciplines under file number B06006, and the Program for Changjiang Scholars and Innovative Research Teams in Universities under file number IRT 0641. Experiments performed at the EPFL were supported by the Swiss National Science Foundation (Project number: 200021_149251). N.G. thanks the European Commission's Framework Project 7 for the financial support through a Marie-Curie Intra-European Fellowship (COCHALPEC, Project 326919). The authors want to thank Dr. Sen Wu (State Key Lab of Precision Measurement Technology and Instruments, Tianjin University) who operated AFM (Dimension ICON, Nanoscope V, Bruker) measurements for us.

■ REFERENCES

(1) Murphy, A. B.; Barnes, P. R. F.; Randeniya, L. K.; Plumb, I. C.; Grey, I. E.; Horne, M. D.; Glasscock, J. A. Efficiency of Solar Water Splitting Using Semiconductor Electrodes. *Int. J. Hydrogen Energy* **2006**, *31*, 1999−2017.

(2) Li, M.; Deng, J. J.; Pu, A. W.; Zhang, P. P.; Zhang, H.; Gao, J.; Hao, Y. Y.; Zhong, J.; Sun, X. H. Hydrogen-Treated Hematite Nanostructures with Low Onset Potential for Highly Efficient Solar Water Oxidation. *J. Mater. Chem. A* **2014**, *2*, 6727−6733.

(3) Hamd, W.; Cobo, S.; Fize, J.; Baldinozzi, G.; Schwartz, W.; Reymermier, M.; Pereira, A.; Fontecave, M.; Artero, V.; Laberty-Robert, C.; Sanchez, C. Mesoporous α-Fe_2O_3 Thin Films Synthesized via The Sol-Gel Process for Light-Driven Water Oxidation. *Phys. Chem. Chem. Phys.* **2012**, *14*, 13224−13232.

(4) Kim, J. Y.; Magesh, G.; Youn, D. H.; Jang, J. W.; Kubota, J.; Domen, K.; Lee, J. S. Single-crystalline, Wormlike Hematite Photoanodes for Efficient Solar Water Splitting. *Sci. Rep.* **2013**, *3*, 2681.

(5) Ling, Y.; Wang, G.; Wheeler, D. A.; Zhang, J. Z.; Li, Y. Sn-Doped Hematite Nanostructures for Photoelectrochemical Water Splitting. *Nano Lett.* **2011**, *11*, 2119−2125.

(6) Deng, J.; Lv, X.; Gao, J.; Pu, A.; Li, M.; Sun, X.; Zhong, J. Facile Synthesis of Carbon-Coated Hematite Nanostructures for Solar Water Splitting. *Energy Environ. Sci.* **2013**, *6*, 1965−1970.

(7) Tilley, S. D.; Cornuz, M.; Sivula, K.; Gratzel, M. Light-Induced Water Splitting with Hematite: Improved Nanostructure and Iridium Oxide Catalysis. *Angew. Chem., Int. Ed.* **2010**, *49*, 6405−6408.

(8) Sivula, K.; Le Formal, F.; Grätzel, M. Solar Water Splitting: Progress Using Hematite (α-Fe_2O_3) Photoelectrodes. *ChemSusChem* **2011**, *4*, 432−449.

(9) Li, Y.; Zhang, X.; Jiang, S.; Dai, H.; Sun, X.; Li, Y. Improved Photoelectrochemical Property of a Nanocomposite NiO/CdS@ZnO Photoanode for Water Splitting. *Sol. Energy Mater. Sol. Cells* **2015**, *132*, 40−46.

(10) Zhang, X.; Li, Y.; Zhao, J.; Wang, S.; Li, Y.; Dai, H.; Sun, X. Advanced Three-Component ZnO/Ag/CdS Nanocomposite Photoanode for Photocatalytic Water Splitting. *J. Power Sources* **2014**, *269*, 466−472.

(11) Lindgren, T.; Wang, H. L.; Beermann, N.; Vayssieres, L.; Hagfeldt, A.; Lindquist, S. E. Aqueous Photoelectrochemistry of Hematite Nanorod Array. *Sol. Energy Mater. Sol. Cells* **2002**, *71*, 231−243.

(12) Ling, Y.; Wang, G.; Wang, H.; Yang, Y.; Li, Y. Low-Temperature Activation of Hematite Nanowires for Photoelectrochemical Water Oxidation. *ChemSusChem* **2014**, *7*, 848−853.

(13) Lee, C. Y.; Wang, L.; Kado, Y.; Killian, M. S.; Schmuki, P. Anodic Nanotubular/Porous Hematite Photoanode for Solar Water Splitting: Substantial Effect of Iron Substrate Purity. *ChemSusChem* **2014**, *7*, 934−940.

(14) Bassi, P. S.; Gurudayal; Wong, L. H.; Barber, J. Iron Based Photoanodes for Solar Fuel Production. *Phys. Chem. Chem. Phys.* **2014**, *16*, 11834−11842.

(15) Lei, Y. F.; Leng, Y. X.; Yang, P.; Wan, G. J.; Huang, N. Theoretical Calculation and Experimental Study of Influence of Oxygen Vacancy on The Electronic Structure and Hemocompatibility of Rutile TiO_2. *Sci. China, Ser. E: Technol. Sci.* **2009**, *52*, 2742−2748.

(16) Deb, S. K. Opportunities and Challenges in Science and Technology of WO_3 for Electrochromic and Related Applications. *Sol. Energy Mater. Sol. Cells* **2008**, *92*, 245−258.

(17) Zandi, O.; Hamann, T. W. Enhanced Water Splitting Efficiency Through Selective Surface State Removal. *J. Phys. Chem. Lett.* **2014**, *5*, 1522−1526.

(18) Hisatomi, T.; Le Formal, F.; Cornuz, M.; Brillet, J.; Tetreault, N.; Sivula, K.; Gratzel, M. Cathodic Shift in Onset Potential of Solar Oxygen Evolution on Hematite by 13-Group Oxide Overlayers. *Energy Environ. Sci.* **2011**, *4*, 2512−2515.

(19) Ling, Y.; Wang, G.; Wheeler, D. A.; Zhang, J. Z.; Li, Y. Sn-Doped Hematite Nanostructures for Photoelectrochemical Water Splitting. *Nano Lett.* **2011**, *11*, 2119−2125.

(20) Frydrych, J.; Machala, L.; Tucek, J.; Siskova, K.; Filip, J.; Pechousek, J.; Safarova, K.; Vondracek, M.; Seo, J. H.; Schneeweiss, O.; Grätzel, M.; Sivula, K.; Zboril, R. Facile Fabrication of Tin-Doped Hematite Photoelectrodes - Effect of Doping on Magnetic Properties and Performance for Light-Induced Water Splitting. *J. Mater. Chem.* **2012**, *22*, 23232−23239.

(21) Brillet, J.; Gratzel, M.; Sivula, K. Decoupling Feature Size and Functionality in Solution-Processed, Porous Hematite Electrodes for Solar Water Splitting. *Nano Lett.* **2010**, *10*, 4155−4160.

(22) Prevot, M. S.; Guijarro, N.; Sivula, K. Enhancing The Performance of A Robust Sol-Gel-Processed p-type Delafossite $CuFeO_2$ Photocathode for Solar Water Reduction. *ChemSusChem* **2015**, *8*, 1359−1367.

(23) Li, Y.; Yu, Z.; Meng, J.; Li, Y. Enhancing The Activity of A SiC-TiO_2 Composite Catalyst for Photo-Stimulated Catalytic Water Splitting. *Int. J. Hydrogen Energy* **2013**, *38*, 3898−3904.

(24) Li, Y.; Zhang, X.; Jiang, S.; Li, Y. In-Depth Investigation of An In-Ni-Ta-O-N Photocatalyst for Overall Water Splitting under Sunlight. *J. Catal.* **2014**, *320*, 208−214.

(25) Hosseini-Zori, M.; Taheri-Nassaj, E. Nano Encapsulation of Hematite into Silica Matrix as A Red Inclusion Ceramic Pigment. *J. Alloys Compd.* **2012**, *510*, 83−86.

(26) Guo, Q.; Ford, G. M.; Agrawal, R.; Hillhouse, H. W. Ink Formulation and Low-Temperature Incorporation of Sodium to Yield

12% Efficient Cu(In,Ga)(S,Se)$_2$ Solar Cells From Sulfide Nanocrystal Inks. *Prog. Photovoltaics* **2013**, *21*, 64−71.

(27) Sivula, K.; Zboril, R.; Le Formal, F.; Robert, R.; Weidenkaff, A.; Tucek, J.; Frydrych, J.; Gratzel, M. Photoelectrochemical Water Splitting With Mesoporous Hematite Prepared by A Solution-Based Colloidal Approach. *J. Am. Chem. Soc.* **2010**, *132*, 7436−7444.

(28) Frydrych, J.; Machala, L.; Tucek, J.; Siskova, K.; Filip, J.; Pechousek, J.; Safarova, K.; Vondracek, M.; Seo, J.-H.; Schneeweiss, O.; Grätzel, M.; Sivula, K.; Zboril, R. Facile fabrication of tin-doped hematite photoelectrodes − effect of doping on magnetic properties and performance for light-induced water splitting. *J. Mater. Chem.* **2012**, *22*, 23232−23239.

(29) Li, Y.; Zhang, X.; Chen, H.; Li, Y. Thermal Conversion Synthesis of Cu$_2$O Photocathode and The Promoting Effects of Carbon Coating. *Catal. Commun.* **2015**, *66*, 1−5.

(30) Tilley, S. D.; Cornuz, M.; Sivula, K.; Gratzel, M. Light-Induced Water Splitting with Hematite: Improved Nanostructure and Iridium Oxide Catalysis. *Angew. Chem., Int. Ed.* **2010**, *49*, 6405−6408.

(31) Miyake, H.; Kozuka, H. Photoelectrochemical Properties of Fe$_2$O$_3$-Nb$_2$O$_5$ Films Prepared by Sol-Gel Method. *J. Phys. Chem. B* **2005**, *109*, 17951−17956.

(32) Wang, H.; Turner, J. A. Characterization of Hematite Thin Films for Photoelectrochemical Water Splitting in a Dual Photoelectrode Device. *J. Electrochem. Soc.* **2010**, *157*, F173−F178.

(33) Poruba, A.; Fejfar, A.; Remeš, Z.; Špringer, J.; Vaněček, M.; Kočka, J.; Meier, J.; Torres, P.; Shah, A. Optical Absorption and Light Scattering in Microcrystalline Silicon Thin Films and Solar Cells. *J. Appl. Phys.* **2000**, *88*, 148−160.

(34) Lian, X. J.; Yang, X.; Liu, S. J.; Xu, Y.; Jiang, C. P.; Chen, J. W.; Wang, R. L. Enhanced Photoelectrochemical Performance of Ti-Doped Hematite Thin Films Prepared by The Sol-Gel Method. *Appl. Surf. Sci.* **2012**, *258*, 2307−2311.

(35) Herrmann-Geppert, I.; Bogdanoff, P.; Radnik, J.; Fengler, S.; Dittrich, T.; Fiechter, S. Surface Aspects of Sol-Gel Derived Hematite Films for The Photoelectrochemical Oxidation of Water. *Phys. Chem. Chem. Phys.* **2013**, *15*, 1389−1398.

(36) Lu, X.; Zeng, Y.; Yu, M.; Zhai, T.; Liang, C.; Xie, S.; Balogun, M. S.; Tong, Y. Oxygen-Deficient Hematite Nanorods as High-Performance and Novel Negative Electrodes for Flexible Asymmetric Supercapacitors. *Adv. Mater.* **2014**, *26*, 3148−3155.

(37) Ling, Y.; Wang, G.; Wang, H.; Yang, Y.; Li, Y. Low-Temperature Activation of Hematite Nanowires for Photoelectrochemical Water Oxidation. *ChemSusChem* **2014**, *7*, 848−853.

(38) Franking, R.; Li, L. S.; Lukowski, M. A.; Meng, F.; Tan, Y. Z.; Hamers, R. J.; Jin, S. Facile Post-Growth Doping of Nanostructured Hematite Photoanodes for Enhanced Photoelectrochemical Water Oxidation. *Energy Environ. Sci.* **2013**, *6*, 500−512.

(39) Kim, T. H.; Kim, H. S.; Hwang, I. C.; Yoon, K. B. Effect of Metal Doping, Doped Structure, and Annealing under Argon on The Properties of 30 nm Thick Ultrathin Hematite Photoanodes. *Phys. Chem. Chem. Phys.* **2014**, *16*, 21936−21940.

(40) Lopes, T.; Andrade, L.; Le Formal, F.; Gratzel, M.; Sivula, K.; Mendes, A. Hematite Photoelectrodes for Water Splitting: Evaluation of The Role of Film Thickness by Impedance Spectroscopy. *Phys. Chem. Chem. Phys.* **2014**, *16*, 16515−16523.

(41) Klahr, B.; Gimenez, S.; Fabregat-Santiago, F.; Bisquert, J.; Hamann, T. W. Electrochemical and Photoelectrochemical Investigation of Water Oxidation with Hematite Electrodes. *Energy Environ. Sci.* **2012**, *5*, 7626−7636.

(42) Le Formal, F.; Tétreault, N.; Cornuz, M.; Moehl, T.; Grätzel, M.; Sivula, K. Passivating Surface States on Water Splitting Hematite Photoanodes With Alumina Overlayers. *Chem. Sci.* **2011**, *2*, 737−743.

(43) Moussy, J.-B. From epitaxial growth of ferrite thin films to spin-polarized tunnelling. *J. Phys. D: Appl. Phys.* **2013**, *46*, 143001.

(44) Le Formal, F.; Pendlebury, S. R.; Cornuz, M.; Tilley, S. D.; Grätzel, M.; Durrant, J. R. Back Electron-hole Recombination in Hematite Photoanodes for Water Splitting. *J. Am. Chem. Soc.* **2014**, *136*, 2564−2574.

(45) Le Formal, F.; Pastor, E.; Tilley, S. D.; Mesa, C. A.; Pendlebury, S. R.; Grätzel, M.; Durrant, J. R. Rate Law Analysis of Water Oxidation on a Hematite Surface. *J. Am. Chem. Soc.* **2015**, *137*, 6629−6637.